

Fast fabrication of WS₂/Bi₂Se₃ heterostructure for high-performance photodetection

Fan Li¹, Jialin Li¹, Junsheng Zheng¹, Yuanbiao Tong¹, Huanfeng Zhu^{1,2}, Pan Wang^{1,2}, and Linjun Li^{1,2}*

Author Information

Corresponding Author

Linjun Li – 1. State Key Laboratory of Modern Optical Instrumentation, College of Optical Science and Engineering, Hangzhou 310000, R. P. China; Email: lilingjun@zju.edu.cn

2. Intelligent Optics & Photonics Research Center, Jiaying Research Institute Zhejiang University, Jiaying 314000, China

Authors

Fan Li - State Key Laboratory of Modern Optical Instrumentation, College of Optical Science and Engineering, Hangzhou 310000, R. P. China

Jialin Li - State Key Laboratory of Modern Optical Instrumentation, College of Optical Science and Engineering, Hangzhou 310000, R. P. China

Junsheng Zheng - State Key Laboratory of Modern Optical Instrumentation, College of Optical Science and Engineering, Hangzhou 310000, R. P. China

Yuanbiao Tong - State Key Laboratory of Modern Optical Instrumentation, College of Optical Science and Engineering, Hangzhou 310000, R. P. China

Huanfeng Zhu – 1. State Key Laboratory of Modern Optical Instrumentation, College of Optical Science and Engineering, Hangzhou 310000, R. P. China

2. Intelligent Optics & Photonics Research Center, Jiaying Research Institute Zhejiang University, Jiaying 314000, China

Pan Wang – 1. State Key Laboratory of Modern Optical Instrumentation, College of Optical Science and Engineering, Hangzhou 310000, R. P. China

2. Intelligent Optics & Photonics Research Center, Jiaying Research Institute Zhejiang University, Jiaying 314000, China

Keywords: 2D materials, van der Waals heterostructures, fast transfer, WS₂/Bi₂Se₃,

photodetectors

Abstract

Two-dimensional (2D) material heterostructures have attracted considerable attention owing to their interesting and novel physical properties which expand the possibilities for future optoelectronic, photovoltaic and nanoelectronic applications. A portable, fast and deterministic transfer technique is highly needed for the fabrication of heterostructures. Herein, we report a fast half-wet polydimethylsiloxane (PDMS) transfer process utilizing the change of adhesion energy with the help of micron sized water droplets. Using this method, a vertical stacking of WS₂/Bi₂Se₃ heterostructure with a straddling band configuration is successfully assembled on fluorophlogopite substrate. Thanks to the complementary bandgaps and high efficiency of interfacial charge-transfer, the photodetector based on the heterostructure exhibits a superior responsivity of 109.9 A W⁻¹ for a visible incident light at 473 nm and 26.7 A W⁻¹ for a 1064 nm near-infrared illumination. Such high photoresponsivity of the heterostructure demonstrates that our transfer method not only owns time efficiency but also ensures high quality of the heterointerface. Our study may open new pathways to the fast and massive fabrication of various vertical 2D heterostructures for applications in twistrionics/valleytronics and other band engineering devices.

Introduction

Van der Waals (vdW) heterostructures based on vertically stacked two-dimensional (2D) materials have been widely studied owing to their synergistic role that improving the functional characteristics.^{1, 2} New functionalities can arise from the interface between dissimilar 2D materials, or from the differences of their electronic structures, lattice constants and Young's modulus, creating quantum wells, twisted superlattices, strong light-matter interaction and superior optoelectronic properties.³⁻⁶

There have been extensive reports on methods of producing 2D heterostructures, which can be divided into two directions: in situ direct growth and multistep mechanical transfer.

In situ direct growth means direct growth of different layers sequentially. The general

techniques, such as molecular beam epitaxy (MBE), physical vapor deposition (PVD), pulsed laser deposition (PLD), and chemical vapor deposition (CVD) for monolayer growth, can be slightly modified to realize the direct fabrication of heterostructures.⁷⁻¹⁰ MBE potentially allows precise control over elemental deposition rates and easy switching from one material to another, enabling the fabrication of the heterostructures on wafer-scales. Several kinds of heterostructures have been reported, like MoTe₂/MoS₂, MoSe₂/HfSe₂ and Bi₂Se₃/graphene, via one-step growth or in situ growth on the bottom material.¹¹⁻¹⁴ PVD offers many advantages such as selective and large-area growth, high growth rate and low cost. WS₂/MoS₂ heterojunction can be assembled via reactive sputtering deposition (RSD), which is one type of PVD.⁹ Moreover, PLD is also a type of PVD methods, which is precursor free and provides controllable growth rate and sample thickness via changing the energy fluence of the pulsed laser. A few reports demonstrate this large-area growth technology, WS₂/Bi₂Te₃ heterostructure and WS₂/WSe₂/WS₂ tri-layer heterostructure have been fabricated and demonstrate great performance in photodetection and quantum well, respectively.^{8, 15} CVD is an efficient and scalable method in the preparation of monolayer and bilayer 2D materials, which is also an alternative choice for the fabrication of heterostructures.¹⁶ Gong et al. achieved direct growth of MoS₂/WS₂ heterostructures on SiO₂/Si substrate.⁷ Several other van der Waals heterostructures, such as MoS₂/WSe₂, MoS₂/CdS, WSe₂/SnS₂ have been successfully synthesized by the CVD method.¹⁷⁻¹⁹ Although in situ growth technology has plenty of advantages, like large scale, considerable productivity and low cost, it is still confronted with certain challenges. Firstly, the construction of the heterostructures, like the twist angle between two layers, is fixed by the self-assembly process.¹⁰ Furthermore, the random position growth leads to low reproducibility. Secondly, it is hard to satisfy the growth conditions of the two target materials simultaneously, such as growth temperature and gas atmosphere, which limits the categories of heterostructures that in situ direct growth can achieve.²⁰

As a result, traditional mechanical transfer methods still have irreplaceable advantages. The pick-drop process has almost no restrictions on the categories of the target samples. In some degree, every two types of thin film materials could be combined and form a heterostructure. Moreover, this technique provides controllable precise stacking alignment, which makes near-

zero twisted heterostructures possible.⁴ One of the most commonly reported methods is the polymethylmethacrylate (PMMA) film based wet transfer, which uses a PMMA film spin-coated on substrates as an adhesion layer and support.²¹ Utilizing the contrast between hydrophilic and hydrophobic of PMMA and growth substrate or using corrosive solvent (like NaOH or HF aqueous solution) to separate substrates and PMMA adhered with target material. The whole PMMA film can be placed onto another target substrate and after dissolving PMMA, the target material remains on the substrate and the transfer finishes.²² However, the PMMA is hard to be dissolved completely and the residue remaining on the sample degrades its device performance and limits its potential applications. Moreover, the wrinkling of the PMMA film cannot be avoided, which makes precise placement challenging and brings unwanted deformation of the sample. Another general method via the viscosity of polydimethylsiloxane (PDMS) can easily pick up mechanically exfoliated flakes and release the flakes by stronger van der Waals force between flakes and the bottom substrate or sample.²³ Nevertheless, it's hard for PDMS to pick up samples grown by CVD because of the robust adhesion between samples and the rigid grown substrate. Other effective transfer methods have been reported such as using a polypropylene carbonate (PPC) coated PDMS block as the transfer support or polymer support/Graphene/target substrate roll-to roll transfer.^{24, 25} These methods either involve residues or have difficulty on picking up CVD grown flakes. Due to current status, there is still urgent need to develop a clean, fast and easy aligning transfer method to fabrication of vdW heterostructures exploiting the massively CVD grown materials.

Herein, we report a fast half-wet PDMS transfer method that utilizes the change of adhesion energy with the help of hot water vapor and compare the complexity of different grown substrates. In previous reports, X. Ma et al. explored the assisted effect of capillary force induced by water vapor and successfully transferred graphene and MoS₂ domains grown on SiO₂/Si wafer. But they didn't explore the applicability of this method in other substrate, such as sapphire and mica. Also, it lacks fine control of material placement in an in situ manner and more precise transfer manipulation is needed for large scale monolayer.²⁶ Lee et al. achieved high quality graphene transfer from an Al₂O₃ substrate via deionized (DI) water, while Y. Hou et al. utilized similar method to fabricate twisted bilayer graphene.^{27, 28} However, they both

focused on mechanical exfoliated graphene and a pretreated step was needed, while samples grown by CVD were still neglected. S. Dong et al. expanded the transfer method to transition metal dichalcogenides (TMD) grown by CVD via assistance of hot DI water, which was induced by pipette or directly dipping PDMS/sample in water.²⁹ In this process, plenty of water was needed, resulting in long time to dry PDMS and large area of monolayer was unable to be transferred because of the wrinkles caused by water. J. Cai et al. also used trapezoid PDMS and water droplets to transfer WS₂ flakes, while the size of the transferred flakes was limited to a few microns.³⁰ Compared to previously reported methods, our method not only combines their advantages, but also explores the applicability to different substrates (such as sapphire and mica) and realizes the transfer of large-area single monolayer flakes. With the assistance of micro sized water droplets instead of spraying or immersion in water, PDMS can be switched from wet to dry in seconds, which promotes the efficiency of transfer and maintaining the original flatness of large monolayer. The whole transfer process can be accompanied in a few minutes.

Furthermore, we fabricate a WS₂/Bi₂Se₃ heterostructure for photodetection via our new method and CVD/PVD grown flakes. The heterostructure with a type-I band alignment shows an excellent photodetection performance from visible to near-infrared illumination. The response parameters of the resultant device are superior to that of the previous reports. For example, the responsivity of our device is 74.5 AW⁻¹ at visible 532 nm light illumination, which is 10³ higher than MoS₂/WS₂ heterostructure, while the responsivity at near-infrared 1064 nm is nearly 2.7×10⁴ higher than WS₂/Bi₂O₂Se device.^{10, 31} Besides, the on/off ratio of 1.06×10⁶ and 7.2×10⁴ at 473 nm and 1064 nm respectively, is 1.7×10³ higher than that of reported WSe₂/Bi₂O₂Se structure.³² The response speed at visible illumination of our device is 18 times faster than previous WS₂/Bi₂Se₃ heterostructure grown by PVD.³³ such outstanding performance manifests that our methodology has potential applications in fast and massive fabrications for high quality functional heterostructure devices and twistrionics/valleytronics.

Results and discussion

Fast half-wet transfer process

The heterostructure is assembled by a fast half-wet transfer process as mentioned above. The

basic procedure of the transfer process is illustrated in **Figure 1**. The setup is developed consisting of a glass slide mounted on a micromanipulator, a bottom stage with translation capability and an optical microscope for visualization. First, a small piece of PDMS is cut and stuck onto a glass slide for adhesion and support. A flask filled with hot water (80 °C) is placed below PDMS and kept for about 10 seconds. The hot vapor condenses on PDMS and forms micro droplets. Then fresh monolayer WS₂ grown on a sapphire substrate is moved to the bottom of PDMS by the translation stage and a suitable WS₂ sample is selected by the microscope. After achieving contact between PDMS and the sapphire by lifting off the glass slide, the droplets penetrate into the interface and decrease the adhesion energy of WS₂ on the sapphire, which make it easier for PDMS to pick WS₂ up. The PDMS moves up with picked WS₂, the sapphire is replaced by the target mica with PVD grown Bi₂Se₃ flakes. By employing the microscope imaging and 3-axis micromanipulator stage, monolayer WS₂ is moved to the aligned location and dropped onto the Bi₂Se₃ slowly and softly. Finally, by careful manipulation through the z-motion of the glass slide-carrying stage, PDMS is peeled off from the mica and monolayer WS₂ remains on Bi₂Se₃ because of van der Waals attracting force. The optical images of the corresponding transfer steps are shown in Figure S1 and S2. In order to tightly combine these two materials, the heterostructure is put into the glove box and annealed at 150 °C for 30 minutes. The final fabrication of WS₂/Bi₂Se₃ heterostructure device is completed via standard electron-beam lithography, with the 5/75 nm Cr/Au electrodes deposited by thermal evaporation.

During the transfer process, the micron sized droplets evaporate quickly, making it easier to precisely drop WS₂ and avoiding wrinkling of the monolayer flake. As a result, no additional steps to dry PDMS are needed, which not only saves time, but also simplifies manipulation and avoids possible folding of monolayer WS₂. In the present setup, only the chosen area of WS₂ is taken up by the transfer process, while the rest of the substrate area remains intact and is preserved for next transfer process, leading to efficient utilization of WS₂. Overall, we compared the half-wet transfer method to several reported transfer techniques with an emphasis on the optimization of the potential limitations of those methods, as shown in **Table 1**.

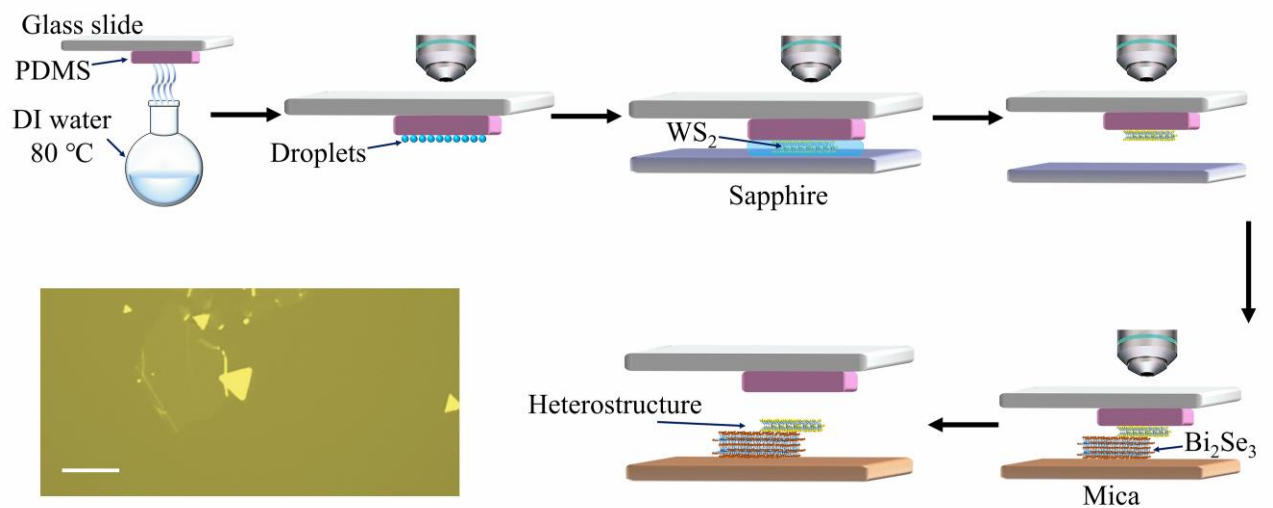


Figure 1. Schematic diagram of the transfer and construction processes of WS_2/Bi_2Se_3 heterostructure, inset: optical image of the fabricated heterostructure (scale bar 10 μm).

Table 1. Transfer performance comparison of this work with previously reported techniques

Work	Transfer process	Evaluation			
		Time consumption	Stacking precision	Sample retaining	Utilization efficiency
C. R. Dean et al. ²¹ Q. Fu et al. ²²	PMMA support film with acetone etching	Overnight soaking to remove PMMA	Hard to locate monolayer on pleated PMMA	Some solvent (like HF) may etch monolayer	Selective transfer of a picked region is not feasible
A. C.-Gomez et al. ²³	All-dry viscoelastic stamping via Gelfilm	In a few minutes	Precise alignment via optical microscope	No residual induced	Only for mechanically exfoliated materials
F. Pizzocchero et al. ²⁴	PPC coated PDMS block as transfer support	In a few minutes	Precise alignment via optical microscope	Heating (over 100 °C) in atmosphere results in oxidation	Only for mechanically exfoliated materials
Z. Juang et al. ²⁵	Roll-to-roll transfer from Ni foil to viscous polymer support film	Rolling speed does not contribute to the transfer results	Not considered	Heating (over 150 °C) in atmosphere results in oxidation and curling produces folds	Selective transfer of a picked region is not feasible and targeted sample is finite
X. Ma et al. ²⁶	Capillary-force-assisted transfer	In a few minutes	Absence of fine control of sample placement in an in situ manner	No additional pollution	Absence of flexibility in controlling area sizes
Lee et al. ²⁷ Y. Hou et al. ²⁸	Pre-treated substrate and PDMS transfer	In a few minutes	Precise alignment via optical microscope	No additional pollution	Only for mechanically exfoliated materials

					and the size of transferred sample is less than 30 μm
S. Dong et al. ²⁹ J. Cai et al. ³⁰	Hot water infiltration assisted PDMS transfer	A certain amount of time needed to immerse and evaporate water	Precise alignment via optical microscope	No additional pollution	The size of transferred materials is a few tens of micrometers
This work	Half-wet transfer method	In a few minutes	Precise alignment via optical microscope	No additional pollution	Good versatility for various types of 2D materials grown on various substrates; flexibility in selecting specific samples and the transferred size up to nearly hundred micrometers

It is worth noting that, compared with other reported transfer results, our half-wet transfer process can pick up single monolayer flake with larger size, up to $\sim 100 \mu\text{m}$ (shown in Figure S3). A. Kozbial et al. theoretically calculated the surface wettability of MoS_2 on SiO_2/Si and found the changes in hydrophilicity of MoS_2 with hydrocarbon absorption.³⁴ S. Dong et al. compared the surface energies of TMDCs and SiO_2 exposed to water with ambient atmosphere and found water-driven separation of TMDC- SiO_2 more energetically favorable.²⁹ J. Cai et al. proposed the water transport model between two surfaces based on the Young-Laplace equation.³⁰ The mechanism of water-assisted transfer should have been unambiguous and universal. However, the results based on previous theories showed limited transfer area, which is inconsistent with ours, meaning extra analysis is needed. We propose that the intercalation of water molecule between WS_2 and sapphire plays an important role in changing adhesion energy. Though direct evidence can be hardly derived for the intercalating process in current stage, the size of water molecule and crystal structure of WS_2 make it comprehensible. According to the previous reported work by Y. Gao et al., the crystal structure of monolayer WS_2 was shown via high-resolution transmission electron microscopy (HRTEM) and the distance between W and S atom is about 3 Å, which form periodic hexagons.³⁵ The size and geometry of water molecule has been widely studied and the length of 2.7 Å is convective.³⁶ These results suggest that water molecule is small enough to go through atomic gap of crystal lattice of WS_2 .³⁷ After water

intercalation and wetting the WS₂/sapphire interface, a large scale monolayer flake can be picked up and the picking speed does not change with the size of transferred flake. Furthermore, we apply half-wet transfer method for different growth substrates, including SiO₂/Si, sapphire and mica, and find that the successful transfer rate for the samples on sapphire is the highest, up to almost 100%.

Characterization of WS₂/Bi₂Se₃ Heterostructure

Figure 2a demonstrates the 3D schematic structure of the WS₂/Bi₂Se₃ heterostructure for photodetection, and an optical microscopic image of the device is provided in **Figure 2b**. Atomic force microscopy (AFM) confirms the thickness across the heterostructure and each individual flake region as shown in **Figure S4**. The thickness line profile implies 1 nm thickness of WS₂ and 8 nm thickness of Bi₂Se₃. With a theoretical thickness of monolayer WS₂ of 0.7 nm and monolayer Bi₂Se₃ of 0.955 nm, this result confirms that our WS₂ flake is monolayer and Bi₂Se₃ flake is about 8-layers.^{38,39} In order to confirm the interfacial coupling effect, room temperature photoluminescence (PL) spectra and mapping were collected from the WS₂/Bi₂Se₃ heterostructure (**Figure 2c, d**). The results indicate that the WS₂ exhibits a strong PL emission peak at 2.01 eV (616 nm), which is comparable to a previously reported value of monolayer WS₂.⁴⁰ The heterostructure region demonstrates an apparent PL quenching effect, as the PL intensity of WS₂ decays to 21% of the pristine and remains only 7% compared with the original after annealing at 150 °C. The evolution of PL change as a function of annealing temperature is shown in **Figure S5**. This suggests the photoexcited carriers are primarily transferred between the WS₂ and Bi₂Se₃ interface, rather than emitting from the individual WS₂ band edges.⁴¹ For the Bi₂Se₃, long-time exposure to air makes its surface oxidation, resulting in the band bending and the change of photodetection performance. Utilizing our fast half-wet transfer method, the time for heterostructure stacking is shortened, just a few minutes. As a result, air exposure time for the whole period of device fabrication can be restricted within 4 hours, meaning that the heterostructure maintains natural properties. Raman spectra of Bi₂Se₃ after fabricating demonstrates three distinct Raman peak positions at 69, 126, and 173 cm⁻¹, corresponding to the A_{1g}¹, E_g² and A_{1g}² modes, respectively, which are in accordance with the previous reports (**Figure 2e**).¹⁴ The in-plane and out-of-plane vibration modes for the individual and overlap

region of WS_2 at 355 and 420 cm^{-1} , respectively, are also shown in Figure 2e. The ratio of the intensities of the A_{1g} and E_{2g}^1 peaks is less than 0.5 , which also indicates its monolayer thickness.⁴² The WS_2 and Bi_2Se_3 characteristic peaks show no shift in the heterostructure, demonstrating that the lattice property of WS_2 and Bi_2Se_3 are not changed after half-wet transfer and thermal annealing.

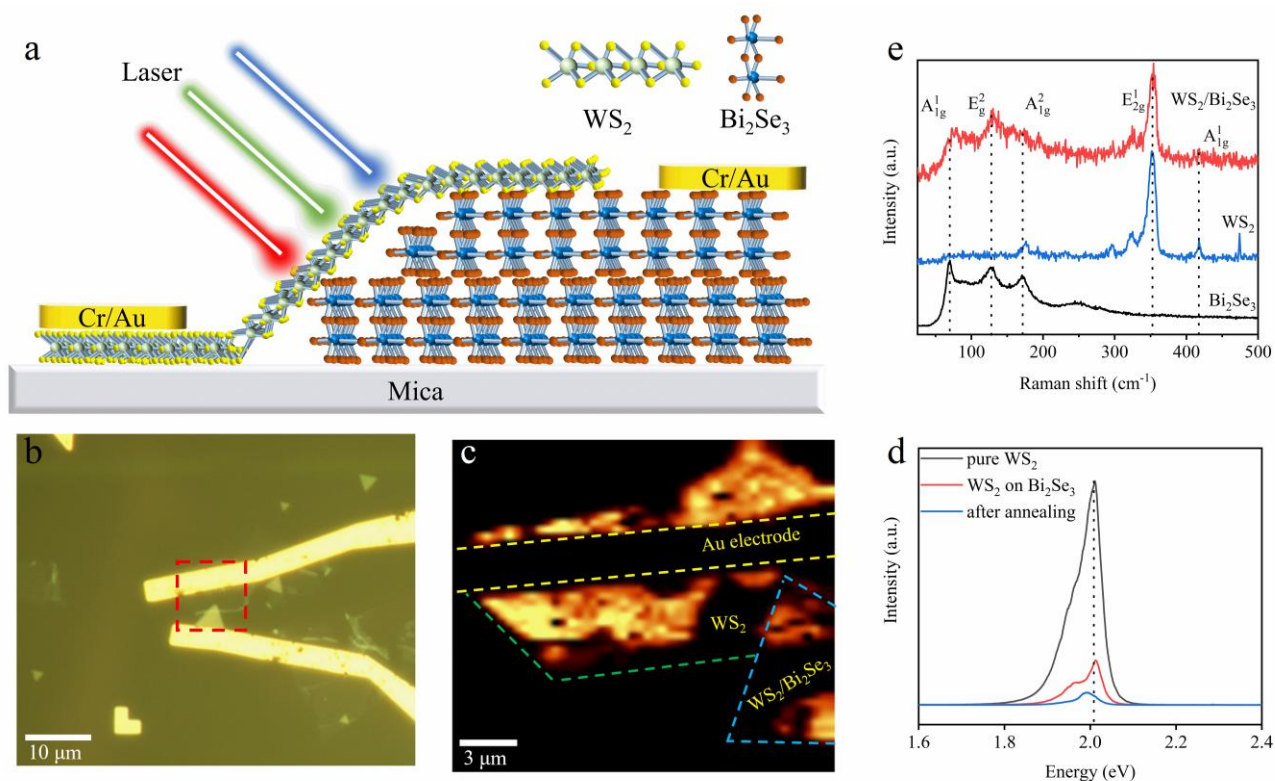


Figure 2. Device structure and optical characterizations. (a) Schematic diagram and (b) Optical image of $\text{WS}_2/\text{Bi}_2\text{Se}_3$ heterostructure device. The monolayer WS_2 is stacked on the top of the Bi_2Se_3 flake. (c) PL mapping of the region surrounded by red dashed lines in Figure 2b. (d) PL spectra measured for WS_2 and the heterostructure. (e) Raman spectra of individual Bi_2Se_3 and $\text{WS}_2/\text{Bi}_2\text{Se}_3$ heterostructure after device fabrication.

Electronic Characteristics of $\text{WS}_2/\text{Bi}_2\text{Se}_3$ Heterostructure

The electric transport characteristics of the heterostructure device were studied to understand the interaction in the overlapped heterojunction region. All results are acquired by applying a drain voltage (V_{ds}) on Bi_2Se_3 with WS_2 being ground. **Figure 3a** presents the current-voltage

(I - V) curves of the $\text{WS}_2/\text{Bi}_2\text{Se}_3$ heterostructure in logarithmic (black) and linear (red) scale with the source/drain bias range of -4 to 4 V in the dark. This device shows a rectification behavior with a calculated rectification factor reaching up to 250. To comprehend the carrier transport behavior of the device, the electronic band alignment of the $\text{WS}_2/\text{Bi}_2\text{Se}_3$ heterostructure is established as shown in Figure 3b. According to the previously reported measurement results and our PL spectrum, the conduction band minimum (E_c), valence band maximum (E_v) and Fermi level (E_f) of the WS_2 (Bi_2Se_3) locate at ~ -3.87 eV (-4.91 eV), -5.88 eV (-5.21 eV) and -4.81 eV (-4.61 eV), respectively.^{42, 43} From the electronic band before contact, the Fermi level of Bi_2Se_3 is higher than that of WS_2 . To prove the band difference, Kelvin probe force microscopy (KPFM) is performed to measure the surface potential of the heterostructure, as shown in Figure S6. Since larger surface potential corresponds to lower work function and thus higher Fermi level, the surface potential of Bi_2Se_3 is higher than that of WS_2 by 0.2 eV, which proves the difference of Fermi level between WS_2 and Bi_2Se_3 .⁴⁴ Under the reverse bias condition, the external bias voltage breaks the unified Fermi level, elevating the energy band on Bi_2Se_3 side and descending the WS_2 side as shown in Figure 3c. When a small negative V_{ds} is applied, the electrons in the Bi_2Se_3 are prevented to drift or tunnel to the conduction band of WS_2 because of the existence of potential barrier. With the increasing of bias, the energy band of WS_2 is further descended, the electrons have the possibility to directly tunnel to WS_2 . Nevertheless, the amount of tunneling electrons is limited due to the degenerated Bi_2Se_3 and the light doped of WS_2 . Tunneling current cannot be significantly higher than the thermionic current, which resulting in a stably low bias current $\approx 6 \times 10^{-12}$ A at -4 V condition. In opposite, the energy band of WS_2 is elevated under forward bias voltage as shown in Figure 3d, which allows the electrons transfer freely from WS_2 to Bi_2Se_3 , resulting in a relatively high current.⁴⁵ Because of the unavoidable surface oxidation of Bi_2Se_3 , there exists a barrier between the interface, leading the “open” voltage slightly shifts. Above all, the $\text{WS}_2/\text{Bi}_2\text{Se}_3$ heterostructure device with a type-I band alignment configuration shows a diode characteristics obviously, indicating that our transfer method ensures high quality of the heterointerface.

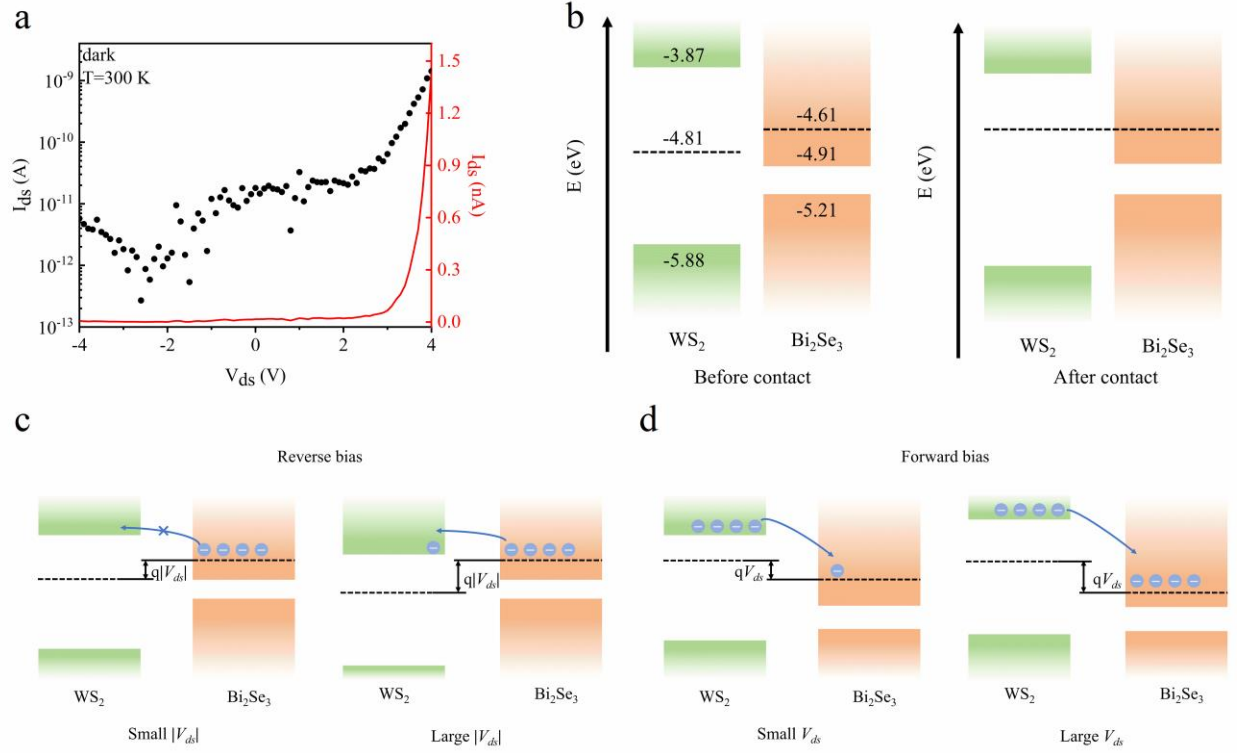


Figure 3. Electronic characteristics of WS₂/Bi₂Se₃ heterostructure. (a) I - V curves of the heterostructure in dark. (b) Energy band diagram of WS₂/Bi₂Se₃ heterostructure before contact and after contact. (c) and (d) Energy band alignment of WS₂/Bi₂Se₃ heterostructure under different bias voltage V_{ds} .

Photoresponse Properties of WS₂/Bi₂Se₃ Heterostructure

Considering the complementary bandgaps of monolayer WS₂ (2.01 eV) and few-layer Bi₂Se₃ (0.3 eV), their heterostructure may exhibit excellent photoresponse performances in both visible and near-infrared regions.^{31, 46} **Figure 4a** shows the I - V curves of the device under dark and different wavelength focused laser illumination with fixed incident power (0.5 mW). Under different condition, the WS₂/Bi₂Se₃ heterostructure shows significant response, demonstrating that the device has a potential in terms of broadband photodetection. Figure 4b, c, d present the output characteristics of the device under 473, 532 and 1064 nm laser light with different power density, respectively. The currents in both forward and reverse biases show increasement with the increase of power density under different laser illumination. In order to evaluate the photodetection performance of the device, the responsivity (R) and specific detectivity (D^*) are calculated. The R value can be calculated by the equation of $R = I_{ph}/(P \cdot S_{eff})$, where I_{ph} , P

and S_{eff} are the photocurrent, incident power density and effective areas of the device, respectively. D^* can be extracted by $D^* = R \cdot \sqrt{S_{\text{eff}}} / \sqrt{2eI_{\text{dark}}}$, where I_{dark} represents the dark current.⁴⁷ Figure 4e, f demonstrate the calculated R and D^* under different laser illumination at different excitation power density, respectively. For visible light of 473 nm, the responsivity reaches up to 109.9 A W^{-1} and the detectivity can get to 3.2×10^{12} Jones at the power density of 4.527 mW cm^{-2} at $V_{\text{ds}} = 4 \text{ V}$, while the near-infrared responsivity is up to 26.7 AW^{-1} and detectivity is 7.76×10^{11} Jones, which is superior to most reported near-infrared photodetectors.^{31, 48}

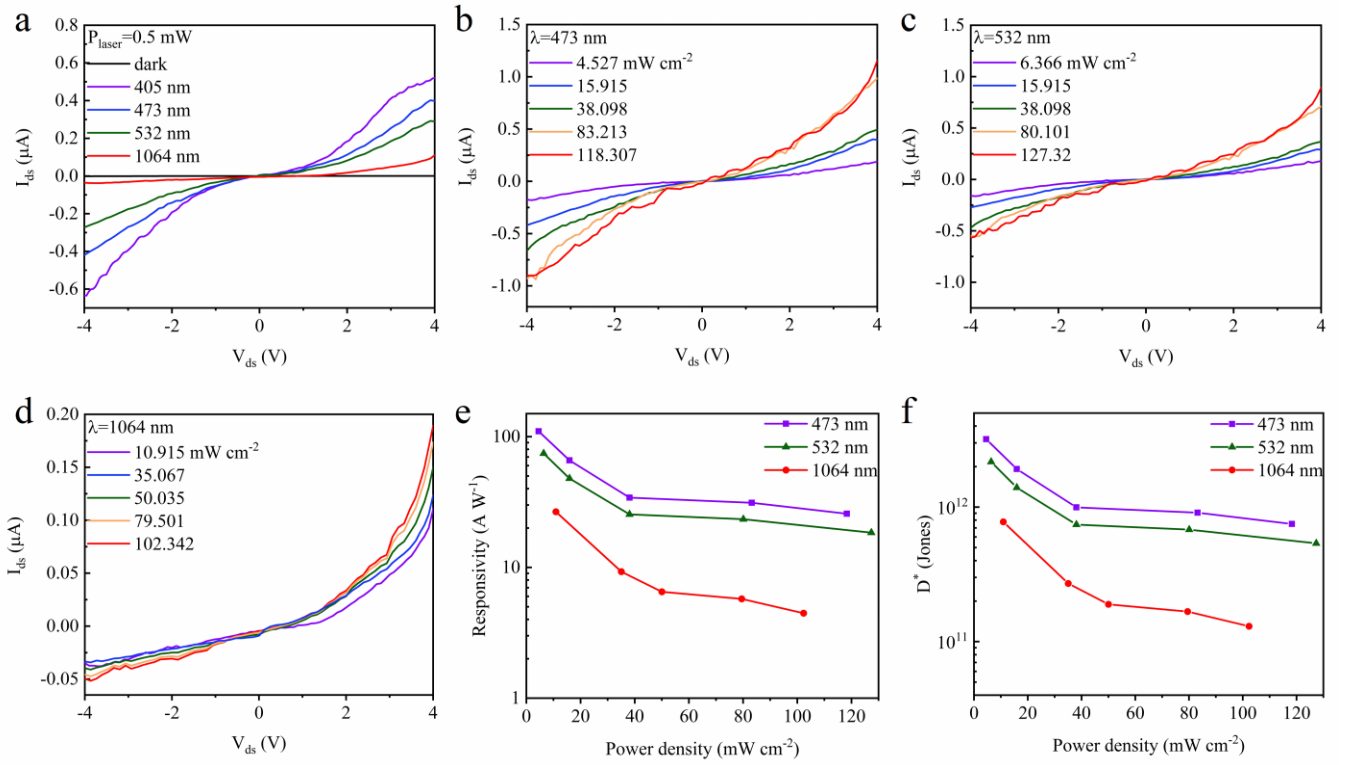


Figure 4. Photoelectric characteristics of WS₂/Bi₂Se₃ heterostructure. (a) Broadband response of the device under different wavelength laser illumination at fixed laser power. (b), (c) and (d) Power depended $I_{\text{ds}}-V_{\text{ds}}$ curves under 473, 532 and 1064 nm laser illumination, respectively. (e) and (f) Power depended R and D^* of the device under different wavelength laser illumination at $V_{\text{ds}}=4 \text{ V}$.

To understand the photocurrent generation mechanism, we further studied the response of the device under reverse and forward bias separately. When the device worked at reverse biases

voltage, we found that the I_{ds} - V_{ds} characteristics could be modeled by the direct tunneling mechanism with linear relationship between $\ln(|I_{ds}|/V_{ds}^2)$ and $\ln(1/|V_{ds}|)$ as shown in **Figure 5a**. This indicates that the photocarriers generated in the WS₂/Bi₂Se₃ heterostructure are dominated by the tunneling mechanism driven by the external reverse electric field. Under visible laser illumination, both WS₂ and Bi₂Se₃ produce photon-generated electron-hole pairs. The barrier height of the heterojunction region becomes smaller, and the electrons can overcome the barrier or direct tunnel, consequently forming considerable photocurrent (Figure 5b). The carriers are generated only in Bi₂Se₃ when illuminated by 1064 nm laser as shown in Figure 5c. The photo-generated holes would enter the circuit, while the photo-generated electrons would accumulate at the interface and tunnel into the conduction band of WS₂, which exhibits a near-infrared photoresponse. From the linear relationship shown in Figure 5a, a formula like $\ln\left(\frac{|I_{ds}|}{V_{ds}^2}\right) = k \ln\left(\frac{1}{V_{ds}}\right) + b$ can be extracted, where k and b are the slope and y-axial offset of the linear fitting line, which is relating to the probability of tunneling.^{49, 50} Then the relationship between photogenerated current and bias voltage can be described as $I_{ds} = e^b \cdot V_{ds}^{2-k}$. From the fitting curves, k_{visible} is smaller than k_{NIR} while b_{visible} is larger than b_{NIR} , meaning a higher photogenerated current under visible illumination, which is consistent with the observed phenomena. By fitting the incident power density (P) dependent current (I_{ph}) through the equation of $I_{ph} \propto P^\alpha$ (Figure 5d), it was found that all the power exponent α values are smaller than 1 under forward bias. This deviation from the ideal value of $\alpha = 1$ suggests a complex process, which relates to the trap states caused by the defects or impurities present in WS₂ or Bi₂Se₃, or the absorbed molecules at WS₂/Bi₂Se₃ interface and slight oxidation on Bi₂Se₃ surface. These factors can trap the photogenerated charges, so that the absorbed photons cannot be completely converted into photocurrent, resulting in the nonlinear photocurrent response.^{51, 52} It can also explain why R and D^* decrease with power density increasing, that is, a drop in the recombination possibility occurs as the photogenerated electrons are captured by the trap states under lower P . The transfer processes of visible and near-infrared photo-generated carriers under forward bias are shown in Figure 5e, f. Moreover, the value of external quantum efficiency (EQE) is another parameter of photodetectors, defined by the ratio of the number of

electrons collected to the number of incident photons. The calculation and the dependence on power density of EQE are shown in Figure S7.⁵³ The WS₂/Bi₂Se₃ heterostructure shows an EQE up to 288.6%, corresponding to the photoconductive gain effect caused by interface trapped states.

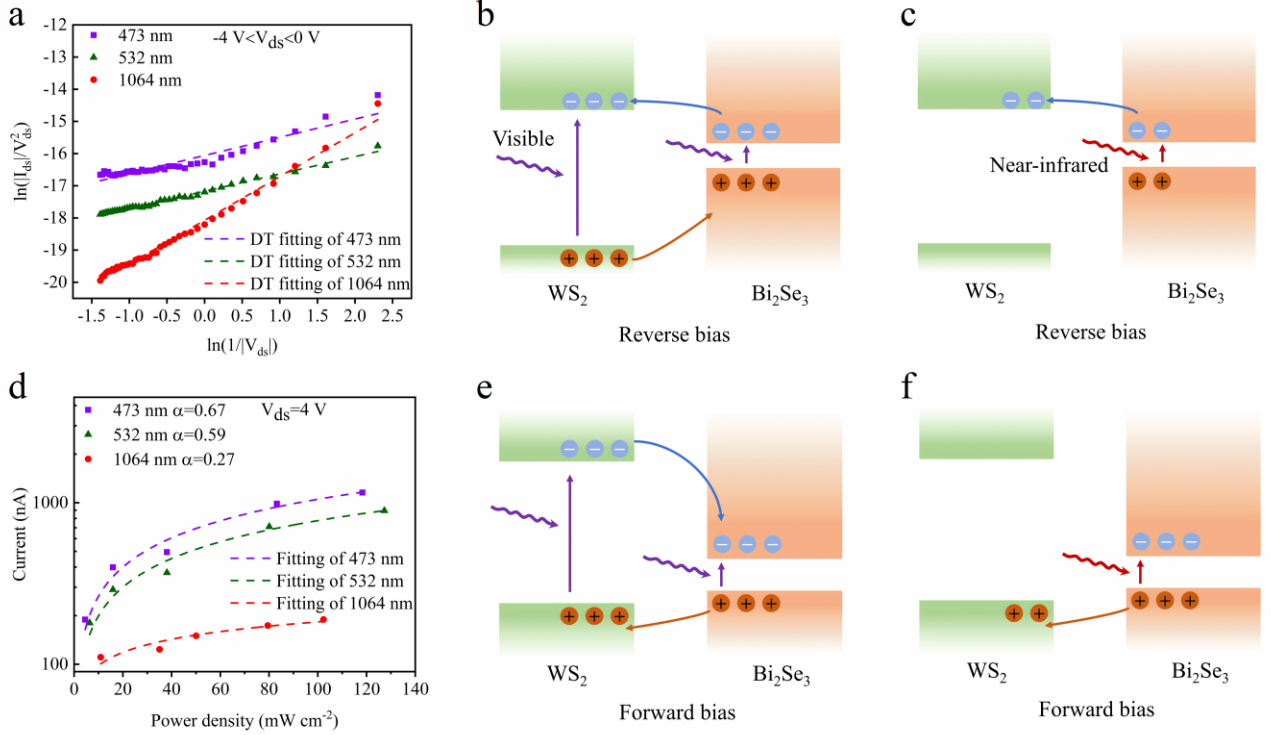


Figure 5. Photocurrent generated mechanism of WS₂/Bi₂Se₃ heterostructure. (a) DT fitting of the device at reverse bias voltage. (b) and (c) Energy band diagram of the heterostructure under reverse bias. (d) The photocurrent dependence of laser power density at $V_{ds}=4 \text{ V}$. (e) and (f) Energy band diagram of the heterostructure under forward bias.

Apart from responsivity, specific detectivity and EQE, response rate and light on/off ratio are also two important parameters for photodetectors. As shown in **Figure 6a**, the WS₂/Bi₂Se₃ heterostructure exhibits well-reproducible photo switching characteristics under different wavelength laser modulation at $V_{ds} = 4 \text{ V}$ and fixed laser power 0.5 W . Furthermore, the light on/off ratio was obtained by comparing the I_{ds} under illumination and dark. The dependence of light on/off ratio on the bias voltage is shown in Figure 6b. Consequently, we obtained the maximum on/off ratio of $\sim 1.06 \times 10^6$ for 473 nm @ $118.307 \text{ mWcm}^{-2}$, 6.3×10^5 for 532 nm @

127.32 mWcm⁻² and 7.2×10^4 for 1064 nm @ 102.342 mWcm⁻² at $V_{ds} = -3$ V. In order to evaluate the ability of charge separation and diffusion, Figure 6c and Figure S8 extracts the rise time (τ_1) and fall time (τ_2) of the WS₂/Bi₂Se₃ heterostructure, which are usually defined as the time requirement of the photocurrent increasing from 10% to 90% and decreasing from 90% to 10%, respectively. For 473 nm laser illumination, the rise time and fall time are estimated to be 7 and 3 ms. Moreover, for 1064 nm photoresponse, the rise time of ~13 ms and decay time of ~7 ms are a bit slower than previous reports. The trap state in CVD grown WS₂ and slightly unavoidable oxidation on the surface of Bi₂Se₃ reduce the recombination rate of photo-generated carriers and prolong the life of carriers.⁴³

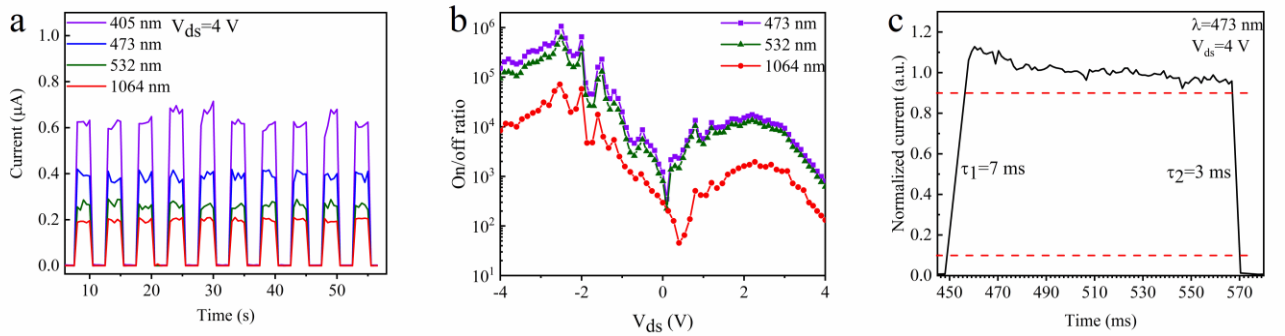


Figure 6. Photoresponse characteristics of the WS₂/Bi₂Se₃ heterostructure. (a) Long-cycle stability measurement of the heterostructure device under different wavelength laser illumination. (b) Light on/off ratio as a function of bias voltage under 473 nm@118.307 mW cm⁻², 532 nm@127.32 mW cm⁻² and 1064 nm@102.342 mW cm⁻². (c) Response time curve of the heterostructure under 473 nm laser illumination.

Finally, we make a comparison of our device with similar vdW heterostructures recently reported on the performances of photodetection, as shown in **Table 2**. There are some other photodetection devices we have fabricated performing similarly, as shown in Figure S9 and S10. One can observe that our WS₂/Bi₂Se₃ heterostructure is highly comparable to the state-of-the-art previously reported photodetection materials, suggesting that our transfer method is a promising way for the future fast and massive fabrication of multifunctional heterostructures.

Table 2. Photodetection performance comparison of this work with similar devices

Device structure	Fabrication method	Wavelength [nm]	Bias [V]	Responsivity [A W ⁻¹]	Detectivity [Jones]	Response rate	On/off ratio
MoS ₂ /WS ₂ ¹⁰	CVD growth	532	1	0.068	—	35/36 ms	—
Bi ₂ Se ₃ /graphene ¹⁴	MBE growth	520	1.5	1.4	—	—/114.94 ms	—
Bi ₂ O ₂ Se/WS ₂ ³¹	PS ^{b)} wet transfer	532	5	0.628	9.5×10 ⁸	33/38 ms	160
		1350	5	0.001	—	—	—
Bi ₂ O ₂ Se/WSe ₂ ³²	PVA dry transfer	635	1	44	3.0×10 ¹³	20/20 ms	1.2×10 ⁴
		1064	1	0.01	2×10 ⁸	—	—
WS ₂ /Bi ₂ Se ₃ ³³	PVD growth	532	1 (V _g = -20)	—	—	126/162 ms	—
Bi ₂ Se ₃ /WSe ₂ ⁴³	PDMS dry transfer	532	-5	94.26	7.9×10 ¹²	1.5/0.11 ms	7.5×10 ⁵
		1456	-5	3	2.2×10 ¹⁰	4/4 ms	3.5×10 ⁴
Bi ₂ O ₂ Se/BP ⁴⁸	PDMS dry transfer	700	-1	500	2.8×10 ¹¹	—/9 ms	—
		1310	-1	4.3	2.4×10 ⁹	—	—
WS ₂ ⁵¹	PVA ^{a)} dry transfer	405	-2	3.45	—	31.78/19.81 ms	—
WSe ₂ /Bi ₂ O ₂ Se ⁵⁴	PDMS dry transfer	532	5	443.83	—	2.4/2.6 μs	1.48
			-5	0.638	—	618	
Bi ₂ O ₂ Se/MoSe ₂ ⁵⁵	PMMA wet transfer	780	2	0.4131	3.7×10 ¹¹	0.79/0.49 s	—
GaSe/graphene ⁵⁶	MBE growth	532	-2	98	3.1×10 ¹²	3/3 ms	10
			4	109.9	3.2×10 ¹²	7/3 ms	1.06×10 ⁶
WS ₂ /Bi ₂ Se ₃ (this work)	half-wet transfer	473 1064	4 4	26.7	7.7×10 ¹¹	13/7 ms	7.2×10 ⁴

^{a)}(poly vinyl alcohol); ^{b)}(polystyrene)

Conclusion

In summary, our study presents a novel 2D material transfer method. By utilizing PDMS and DI water as transfer substrate and lubricant, we successfully realize convenient and fast pick-and-drop process of monolayer WS₂. The size of single transferred monolayer piece is up to hundred-micron scale, which is an order of magnitude higher than the original report. To prove the clean and nondestructive transfer process, we fabricate a high quality WS₂/Bi₂Se₃

heterostructure for photodetection. Our heterostructure with type- I band alignment demonstrates wide spectrum response from visible light to near-infrared band (from 405 to 1064 nm). The critical parameters of our heterostructures such as responsivity of 109.9 and 26.7 A W⁻¹, light on/off ratio of 1.06×10⁶ and 7.2×10⁴ with a fast response time of 7 and 13 ms are obtained at both visible 473 and near-infrared 1064 nm, respectively. Such superior performance demonstrates that our new transfer method may pave a unique avenue to fabricate manifold 2D heterostructures fast and massively.

Experimental Section

Fabrication of Bi₂Se₃/WS₂ heterostructure: First, monolayer WS₂ was grown on Si/SiO₂ (300 nm) substrates or sapphire (C-plane) by using confined-space chemical vapor deposition at atmospheric pressure.¹⁰ A quartz tube was placed in the center of a horizontal tube furnace (BTF-1200C, Anhui Best Equipment Ltd, China) equipped with an assistant substrate facing upward. The WO₃ power was sprinkled on the surface of the assistant substrate while a target growth substrate was placed on the surface of the quartz tube facing down to the assistant substrate. The distance between the assistant substrate and the target growth substrate was about 1 mm. The sulfur power was put into another quartz tube in the center of another furnace upstream. The distance between W and S source was kept as 40 cm. The temperature of W source was first gradually raised up to 600 °C in 60 min, then it was increased to 830 °C with a rate of 10 °C/min and kept at 830 °C for 10 min. When the temperature of W source reached 780 °C, the sulfur power was heated to 200 °C in 5 min and was kept at 200 °C for 10 min for the growth of monolayer WS₂. Finally, the tube furnace was naturally cooled down to room temperature. Ar was used as the carrier and protective gas at a flow rate of 50 sccm during the whole growth process.

Then, 2D Bi₂Se₃ flakes were grown on fluorphlogopite mica substrate by low pressure physical vapor deposition.⁴⁵ The Bi₂Se₃ power was placed in the center of the furnace equipped with a quartz tube and the fluorphlogopite mica substrates were placed in the downstream 8-11 cm away from center. The temperature of Bi₂Se₃ was first raised up to 590 °C in 30 min and kept at this temperature for 20 min with Ar carrier gas flow of 100 sccm. The pressure of the

furnace was kept at 100 Torr. Finally, the furnace was naturally cooled down to room temperature with a flowing Ar gas.

Next, the monolayer WS₂ was transferred onto the Bi₂Se₃ flake via a piece of PDMS as the supporting membrane and DI water as lubricant. The transfer details of picking and dropping were discussed in Results and Discussion. The alignment process is shown as follows: We selected one Bi₂Se₃ as bottom material and marked its location on the camera screen as we did with WS₂. When both WS₂ and Bi₂Se₃ were settled, by employing the microscope imaging and 3-axis micromanipulator stage, monolayer WS₂ was moved to the aligned location and started to drop onto the Bi₂Se₃. With the slide going down, we checked the position of Bi₂Se₃ from time to time, in order to make sure it still stays at the original position we marked. As distance decreasing, we could see the two materials in the screen till they contacted with each other. Last but not least, by careful manually manipulation through the z-motion of the glass slide-carrying stage, PDMS was peeled off from the mica and monolayer WS₂ remained on Bi₂Se₃ because of van der Waals force. Finally, electrode patterns were defined by typical electron beam lithography (Nova Nanosem 450) and deposited by thermally evaporating 5/75 nm Cr/Au (K.J.Lesker Nano 36 Thermal Evaporator).

Characterizations: Optical microscope (Nikon ECLIPSE LV150N) and AFM (Park NX-10) were utilized to characterize the morphology of the heterostructure. Raman and PL were investigated by a confocal microscope spectrometer (Alpha300R-2018model, WITech Ltd.) together with 532 laser source. EFM test cantilever (PPP-NCSTAu 3M) was used to measure the surface potential to obtain the difference of Fermi levels. The electronic and photoelectric measurements of the Bi₂Se₃/WS₂ heterostructure were performed by using a Keithley 2450 sourcemeter. Power fixed 405-nm laser and power adjustable 473-, 532- and 1064 nm lasers (Changchun New Industries Optoelectronics Technology Ltd.) were used to record the photoelectric response of the heterostructure. The radius of laser spot in visible waveband was about 1 mm, and the radius of laser spot in 1064 nm was approximately 1.2 mm.

Supporting Information

Additional characterization results, including optical image characterization, PL mapping characterization, AFM characterization, KPFM characterization and photodetection performance of additional devices.

Acknowledgements

L. J. Li acknowledges the funding from the state key program (91950205), National Key R&D Program of China (2019YFA0308602), and the general program (12174336) of National Science Foundation of China, the Zhejiang Provincial Natural Science Foundation of China (LR20A040002).

Conflict of Interest

The authors declare no conflict of interest.

Data Availability Statement

The data that support the findings of this study are available from the corresponding author upon reasonable request.

Received:
Revised:
Published online:

References

1. Ohno, Y.; Young, D. K.; Beschoten, B.; Matsukura, F.; Ohno, H.; Awschalom, D. D., Electrical Spin Injection in a Ferromagnetic Semiconductor Heterostructure. *Nature* **1999**, *402*, 790-792.
2. Geim, A. K.; Grigorieva, I. V., Van der Waals Heterostructures. *Nature* **2013**, *499* (7459), 419-425.
3. Pasqual Rivera; Kyle L. Seyler; Hongyi Yu; John R. Schaibley; Jiaqiang Yan; David G. Mandrus; Wang Yao; Xu, X., Valley-Polarized Exciton Dynamics in a 2D Semiconductor

Heterostructure. *Science* **2016**, *351* (6274), 688-691.

4. Cao, Y.; Fatemi, V.; Fang, S.; Watanabe, K.; Taniguchi, T.; Kaxiras, E.; Jarillo-Herrero, P., Unconventional Superconductivity in Magic-Angle Graphene Superlattices. *Nature* **2018**, *556* (7699), 43-50.

5. Alexeev, E. M.; Ruiz-Tijerina, D. A.; Danovich, M.; Hamer, M. J.; Terry, D. J.; Nayak, P. K.; Ahn, S.; Pak, S.; Lee, J.; Sohn, J. I.; Molas, M. R.; Koperski, M.; Watanabe, K.; Taniguchi, T.; Novoselov, K. S.; Gorbachev, R. V.; Shin, H. S.; Fal'ko, V. I.; Tartakovskii, A. I., Resonantly Hybridized Excitons in Moire Superlattices in van der Waals Heterostructures. *Nature* **2019**, *567* (7746), 81-86.

6. Forg, M.; Colombier, L.; Patel, R. K.; Lindlau, J.; Mohite, A. D.; Yamaguchi, H.; Glazov, M. M.; Hunger, D.; Hoge, A., Cavity-Control of Interlayer Excitons in van der Waals Heterostructures. *Nat Commun* **2019**, *10* (1), 3697.

7. Gong, Y.; Lin, J.; Wang, X.; Shi, G.; Lei, S.; Lin, Z.; Zou, X.; Ye, G.; Vajtai, R.; Yakobson, B. I.; Terrones, H.; Terrones, M.; Tay, B. K.; Lou, J.; Pantelides, S. T.; Liu, Z.; Zhou, W.; Ajayan, P. M., Vertical and in-plane Heterostructures from WS₂/MoS₂ Monolayers. *Nat Mater* **2014**, *13* (12), 1135-42.

8. Yao, J.; Zheng, Z.; Yang, G., Layered-Material WS₂/Topological Insulator Bi₂Te₃ Heterostructure Photodetector with Ultrahigh Responsivity in the Range from 370 to 1550 nm. *Journal of Materials Chemistry C* **2016**, *4* (33), 7831-7840.

9. Yang, W.; Kawai, H.; Bosman, M.; Tang, B.; Chai, J.; Tay, W. L.; Yang, J.; Seng, H. L.; Zhu, H.; Gong, H.; Liu, H.; Goh, K. E. J.; Wang, S.; Chi, D., Interlayer Interactions in 2D WS₂/MoS₂ Heterostructures Monolithically Grown by in situ Physical Vapor Deposition. *Nanoscale* **2018**, *10* (48), 22927-22936.

10. Zhang, X.; Huangfu, L.; Gu, Z.; Xiao, S.; Zhou, J.; Nan, H.; Gu, X.; Ostrikov, K. K., Controllable Epitaxial Growth of Large-Area MoS₂/WS₂ Vertical Heterostructures by Confined-Space Chemical Vapor Deposition. *Small* **2021**, *17* (18), 2007312.

11. Aretouli, K. E.; Tsipas, P.; Tsoutsou, D.; Marquez-Velasco, J.; Xenogiannopoulou, E.; Giamini, S. A.; Vassalou, E.; Kelaidis, N.; Dimoulas, A., Two-Dimensional Semiconductor HfSe₂ and MoSe₂/HfSe₂ van der Waals Heterostructures by Molecular Beam Epitaxy. *Applied*

Physics Letters **2015**, *106* (14).

12. Diaz, H. C.; Chaghi, R.; Ma, Y.; Batzill, M., Molecular Beam Epitaxy of the van der Waals Heterostructure MoTe₂ on MoS₂: Phase, Thermal, and Chemical Stability. *2D Materials* **2015**, *2* (4).

13. Hinkle, C., van der Waals Heterostructures Grown by MBE. *the MAR16 Meeting of the American Physical Society* **2015**.

14. Chae, J.; Hong, S.-B.; Kim, D.; Kim, D.-K.; Kim, J.; Jeong, K.; Park, S. H.; Cho, M.-H., Enhancement of Photoresponse in Bi₂Se₃/Graphene Heterostructures by Effective Electron–Hole Separation through Internal Band Bending. *Applied Surface Science* **2021**, *554*.

15. Zatko, V.; Dubois, S. M.; Godel, F.; Carretero, C.; Sander, A.; Collin, S.; Galbiati, M.; Peiro, J.; Panciera, F.; Patriarche, G.; Brus, P.; Servet, B.; Charlier, J. C.; Martin, M. B.; Dlubak, B.; Seneor, P., Band-Gap Landscape Engineering in Large-Scale 2D Semiconductor van der Waals Heterostructures. *ACS Nano* **2021**, *15* (4), 7279-7289.

16. Zhou, J.; Lin, J.; Huang, X.; Zhou, Y.; Chen, Y.; Xia, J.; Wang, H.; Xie, Y.; Yu, H.; Lei, J.; Wu, D.; Liu, F.; Fu, Q.; Zeng, Q.; Hsu, C. H.; Yang, C.; Lu, L.; Yu, T.; Shen, Z.; Lin, H.; Yakobson, B. I.; Liu, Q.; Suenaga, K.; Liu, G.; Liu, Z., A Library of Atomically Thin Metal Chalcogenides. *Nature* **2018**, *556* (7701), 355-359.

17. Yu, J. H.; Lee, H. R.; Hong, S. S.; Kong, D.; Lee, H. W.; Wang, H.; Xiong, F.; Wang, S.; Cui, Y., Vertical Heterostructure of Two-Dimensional MoS₂ and WSe₂ with Vertically Aligned Layers. *Nano Lett* **2015**, *15* (2), 1031-5.

18. Yang, T.; Zheng, B.; Wang, Z.; Xu, T.; Pan, C.; Zou, J.; Zhang, X.; Qi, Z.; Liu, H.; Feng, Y.; Hu, W.; Miao, F.; Sun, L.; Duan, X.; Pan, A., Van der Waals Epitaxial Growth and Optoelectronics of Large-Scale WSe₂/SnS₂ Vertical Bilayer p-n Junctions. *Nat Commun* **2017**, *8* (1), 1906.

19. Weixia Gu; Fan Yang; Chen Wu; Yi Zhang; Shi, M.; Ma, X., Fabrication and Investigation of the Optoelectrical Properties of MoS₂/CdS Heterojunction Solar Cells. *Nanoscale Research Letters* **2014**, *9* (662).

20. Castellanos-Gomez, A.; Duan, X.; Fei, Z.; Gutierrez, H. R.; Huang, Y.; Huang, X.; Quereda, J.; Qian, Q.; Sutter, E.; Sutter, P., Van der Waals Heterostructures. *Nature Reviews*

Methods Primers **2022**, *2* (1).

21. Dean, C. R.; Young, A. F.; Meric, I.; Lee, C.; Wang, L.; Sorgenfrei, S.; Watanabe, K.; Taniguchi, T.; Kim, P.; Shepard, K. L.; Hone, J., Boron Nitride Substrates for High-Quality Graphene Electronics. *Nat Nanotechnol* **2010**, *5* (10), 722-6.
22. Fu, Q.; Zhu, C.; Zhao, X.; Wang, X.; Chaturvedi, A.; Zhu, C.; Wang, X.; Zeng, Q.; Zhou, J.; Liu, F.; Tay, B. K.; Zhang, H.; Pennycook, S. J.; Liu, Z., Ultrasensitive 2D Bi₂O₂Se Phototransistors on Silicon Substrates. *Adv Mater* **2019**, *31* (1), 1804945.
23. Andres Castellanos-Gomez; Michele Buscema; Rianda Molenaar; Vibhor Singh; Laurens Janssen; Zant, H. S. J. v. d.; Steele, G. A., Deterministic Transfer of Two-Dimensional Materials by All-Dry Viscoelastic Stamping. *2D Materials* **2014**, *1* (1).
24. Pizzocchero, F.; Gammelgaard, L.; Jessen, B. S.; Caridad, J. M.; Wang, L.; Hone, J.; Boggild, P.; Booth, T. J., The Hot Pick-up Technique for Batch Assembly of van der Waals Heterostructures. *Nat Commun* **2016**, *7*, 11894.
25. Juang, Z.-Y.; Wu, C.-Y.; Lu, A.-Y.; Su, C.-Y.; Leou, K.-C.; Chen, F.-R.; Tsai, C.-H., Graphene Synthesis by Chemical Vapor Deposition and Transfer by a Roll-to-Roll Process. *Carbon* **2010**, *48* (11), 3169-3174.
26. Ma, X.; Liu, Q.; Xu, D.; Zhu, Y.; Kim, S.; Cui, Y.; Zhong, L.; Liu, M., Capillary-Force-Assisted Clean-Stamp Transfer of Two-Dimensional Materials. *Nano Lett* **2017**, *17* (11), 6961-6967.
27. Jun-Ho Lee; Han-Byeol Lee; Nae Bong Jeong; Do-Hyun Park; Inchul Choi; Chung, H.-J., High-Speed Residue-Free Transfer of Two-Dimensional Materials Using PDMS Stamp and Water Infiltration. *Current Applied Physics* **2020**, *20* (10), 1190-1194.
28. Hou, Y.; Ren, X.; Fan, J.; Wang, G.; Dai, Z.; Jin, C.; Wang, W.; Zhu, Y.; Zhang, S.; Liu, L.; Zhang, Z., Preparation of Twisted Bilayer Graphene via the Wetting Transfer Method. *ACS Appl Mater Interfaces* **2020**, *12* (36), 40958-40967.
29. Dong, S.; Zhang, X.; Nathangari, S. S. P.; Krayev, A.; Zhang, X.; Hwang, J. W.; Ajayan, P. M.; Espinosa, H. D., Facile Fabrication of 2D Material Multilayers and vdW Heterostructures with Multimodal Microscopy and AFM Characterization. *Materials Today* **2022**, *52*, 31-42.
30. Cai, J.; Chen, H.; Ke, Y.; Deng, S., A Capillary-Force-Assisted Transfer for Monolayer

Transition-Metal-Dichalcogenide Crystals with High Utilization. *ACS Nano* **2022**, *16* (9), 15016-15025.

31. Fang, C.; Han, J.; Yu, M.; Liu, W.; Gao, S.; Huang, K., WS₂/Bi₂O₂Se van der Waals Heterostructure with Straddling Band Configuration for High Performances and Broadband Photodetector. *Advanced Materials Interfaces* **2022**, *9* (9).

32. Tao, L.; Li, S.; Yao, B.; Xia, M.; Gao, W.; Yang, Y.; Wang, X.; Huo, N., Raman Anisotropy and Polarization-Sensitive Photodetection in 2D Bi₂O₂Se-WSe₂ Heterostructure. *ACS Omega* **2021**, *6* (50), 34763-34770.

33. She, Y.; Wu, Z.; You, S.; Du, Q.; Chu, X.; Niu, L.; Ding, C.; Zhang, K.; Zhang, L.; Huang, S., Multiple-Dimensionally Controllable Nucleation Sites of Two-Dimensional WS₂/Bi₂Se₃ Heterojunctions Based on Vapor Growth. *ACS Appl Mater Interfaces* **2021**, *13* (13), 15518-15524.

34. Kozbial, A.; Gong, X.; Liu, H.; Li, L., Understanding the Intrinsic Water Wettability of Molybdenum Disulfide (MoS₂). *Langmuir* **2015**, *31* (30), 8429-35.

35. Gao, Y.; Liu, Z.; Sun, D. M.; Huang, L.; Ma, L. P.; Yin, L. C.; Ma, T.; Zhang, Z.; Ma, X. L.; Peng, L. M.; Cheng, H. M.; Ren, W., Large-Area Synthesis of High-Quality and Uniform Monolayer WS₂ on Reusable Au Foils. *Nat Commun* **2015**, *6*, 8569.

36. Huang, Y.; Zhang, X.; Ma, Z.; Li, W.; Zhou, Y.; Zhou, J.; Zheng, W.; Sun, C. Q., Size, Separation, Structural Order, and Mass Density of Molecules Packing in Water and Ice. *Sci Rep* **2013**, *3*, 3005.

37. Kausar, A.; Taherian, R., Electrical Conductivity Behavior of Polymer Nanocomposite with Carbon Nanofillers. In *Electrical Conductivity in Polymer-Based Composites: Experiments, Modelling and Applications*, 2019; pp 41-72.

38. Weijie Zhao; Zohreh Ghorannevis; Leiqiang Chu; Minglin Toh; Christian Kloc; Ping-Heng Tan; Eda, G., Evolution of Electronic Structure in Atomically Thin Sheets of WS₂ and WSe₂. *ACS Nano* **2013**, *7* (1), 791-797.

39. Wang, F.; Li, L.; Huang, W.; Li, L.; Jin, B.; Li, H.; Zhai, T., Submillimeter 2D Bi₂Se₃ Flakes toward High-Performance Infrared Photodetection at Optical Communication Wavelength. *Advanced Functional Materials* **2018**, *28* (33).

40. Yu Zhang; Yanfeng Zhang; Qingqing Ji; Jing Ju; Hongtao Yuan; Donglin Ma; Mengxi Liu; Yubin Chen; Xiuju Song; Harold Y. Hwang; Jianping Shi; Teng Gao; Yi Cui; Liu, Z., Controlled Growth of High-Quality Monolayer WS₂ Layers on Sapphire and Imaging Its Grain Boundary. *ACS Nano* **2013**, *7* (10), 8963-8971.
41. Yu, Y.; Hu, S.; Su, L.; Huang, L.; Liu, Y.; Jin, Z.; Purezky, A. A.; Geohegan, D. B.; Kim, K. W.; Zhang, Y.; Cao, L., Equally Efficient Interlayer Exciton Relaxation and Improved Absorption in Epitaxial and Nonepitaxial MoS₂/WS₂ Heterostructures. *Nano Lett* **2015**, *15* (1), 486-91.
42. Liu, S.; He, D.; Tan, C.; Fu, S.; Han, X.; Huang, M.; Miao, Q.; Zhang, X.; Wang, Y.; Peng, H.; Zhao, H., Charge Transfer Properties of Heterostructures Formed by Bi₂O₂Se and Transition Metal Dichalcogenide Monolayers. *Small* **2022**, *18* (7), e2106078.
43. Wang, F.; Luo, P.; Zhang, Y.; Huang, Y.; Zhang, Q.; Li, Y.; Zhai, T., Band Structure Engineered Tunneling Heterostructures for High-Performance Visible and near-Infrared Photodetection. *Science China Materials* **2020**, *63* (8), 1537-1547.
44. Kun Chen; Xi Wan; Jinxiu Wen; Weiguang Xie; Zhiwen Kang; Xiaoliang Zeng; Huanjun Chen; Xu, J.-B., Electronic Properties of MoS₂/WS₂ Heterostructures Synthesized with Two-Step Lateral Epitaxial Strategy. *ACS Nano* **2015**, *9* (10), 9868–9876.
45. Yu, M.; Fang, C.; Han, J.; Liu, W.; Gao, S.; Huang, K., Construction of Bi₂O₂Se/Bi₂Se₃ Van Der Waals Heterostructures for Self-Powered and Broadband Photodetectors. *ACS Appl Mater Interfaces* **2022**, *14* (11), 13507-13515.
46. Luo, M.; Lu, C.; Liu, Y.; Han, T.; Ge, Y.; Zhou, Y.; Xu, X., Band Alignment of Type-I SnS₂/Bi₂Se₃ and Type-II SnS₂/Bi₂Te₃ van der Waals Heterostructures for Highly Enhanced Photoelectric Responses. *Science China Materials* **2021**, *65* (4), 1000-1011.
47. Xing Zhou; Lin Gan; Wenming Tian; Qi Zhang; Shengye Jin; Huiqiao Li; Yoshio Bando; Dmitri Golberg; Zhai, T., Ultrathin SnSe₂ Flakes Grown by Chemical Vapor Deposition for High-Performance Photodetectors. *Adv Mater* **2015**, *27* (48), 8035-8041.
48. Liu, X.; Wang, W.; Yang, F.; Feng, S.; Hu, Z.; Lu, J.; Ni, Z., Bi₂O₂Se/BP van der Waals Heterojunction for High Performance Broadband Photodetector. *Science China Information Sciences* **2021**, *64* (4).

49. Simmons, J. G., Generalized Formula for the Electric Tunnel Effect between Similar Electrodes Separated by a Thin Insulating Film. *Journal of Applied Physics* **1963**, *34* (6), 1793-1803.
50. Ma, Q.; Andersen, T. I.; Nair, N. L.; Gabor, N. M.; Massicotte, M.; Lui, C. H.; Young, A. F.; Fang, W.; Watanabe, K.; Taniguchi, T.; Kong, J.; Gedik, N.; Koppens, F. H. L.; Jarillo-Herrero, P., Tuning Ultrafast Electron Thermalization Pathways in a van der Waals Heterostructure. *Nature Physics* **2016**, *12* (5), 455-459.
51. Wei Gao; Shuai Zhang; Feng Zhang; Peiting Wen; Li Zhang; Yiming Sun; Hongyu Chen; Zhaoqiang Zheng; Mengmeng Yang; Dongxiang Luo; Nengjie Huo; Li, J., 2D WS₂ Based Asymmetric Schottky Photodetector with High Performance. *Advanced Electronic Materials* **2020**, *7* (7).
52. Wenjing Zhang; Jing-Kai Huang; Chang-Hsiao Chen; Yung-Huang Chang; Yuh-Jen Cheng; Li, L.-J., High-Gain Phototransistors Based on a CVD MoS₂ Monolayer. *Adv Mater* **2013**, *25* (25), 3456-3461.
53. Koppens, F. H.; Mueller, T.; Avouris, P.; Ferrari, A. C.; Vitiello, M. S.; Polini, M., Photodetectors Based on Graphene, Other Two-Dimensional Materials and Hybrid Systems. *Nat Nanotechnol* **2014**, *9* (10), 780-93.
54. Luo, P.; Wang, F.; Qu, J.; Liu, K.; Hu, X.; Liu, K.; Zhai, T., Self-Driven WSe₂/Bi₂O₂Se Van der Waals Heterostructure Photodetectors with High Light on/Off Ratio and Fast Response. *Advanced Functional Materials* **2020**, *31* (8).
55. Yang, T.; Yang, X.; Li, X.; Wang, L.; Liao, L.; Liu, Y.; Chen, K.; Dong, L.; Shan, C.-X., Broadband Photodetection of 2D Bi₂O₂Se–MoSe₂ Heterostructure. *Journal of Materials Science* **2019**, *54* (24), 14742-14751.
56. Saroj, R. K.; Guha, P.; Lee, S.; Yoo, D.; Lee, E.; Lee, J.; Kim, M.; Yi, G. C., Photodetector Arrays Based on MBE-Grown GaSe/Graphene Heterostructure. *Advanced Optical Materials* **2022**.

Support Information

Fast fabrication of WS₂/Bi₂Se₃ heterostructure for high-performance photodetection

Fan Li, Jialin Li, Junsheng Zheng, Yuanbiao Tong, Huanfeng Zhu, Pan Wang, and Linjun Li*

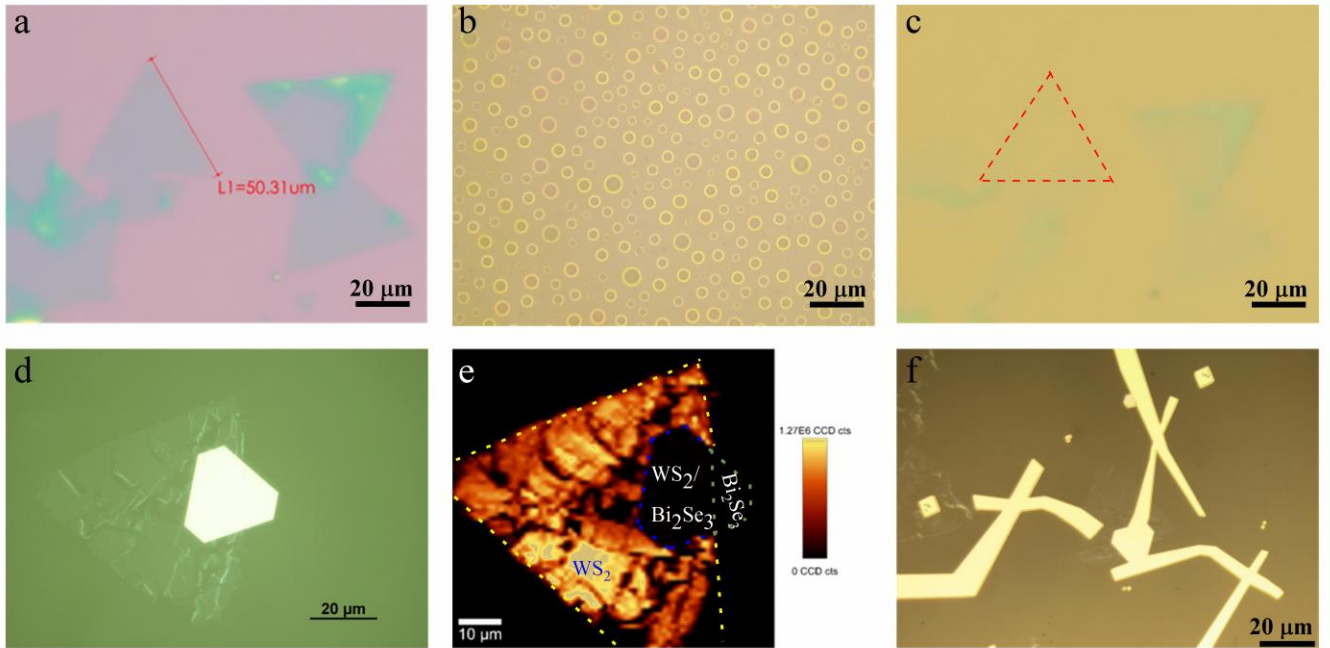


Figure S1. Optical image of half-wet transfer process from SiO₂/Si to mica. (a) Monolayer WS₂ grown on SiO₂/Si. (b) The water droplets liquified on PDMS from hot DI water vapour. (c) WS₂ lifted on PDMS. (d) The WS₂/Bi₂Se₃ heterostructure. (e) PL mapping of the heterostructure. (f) The photodetection device.

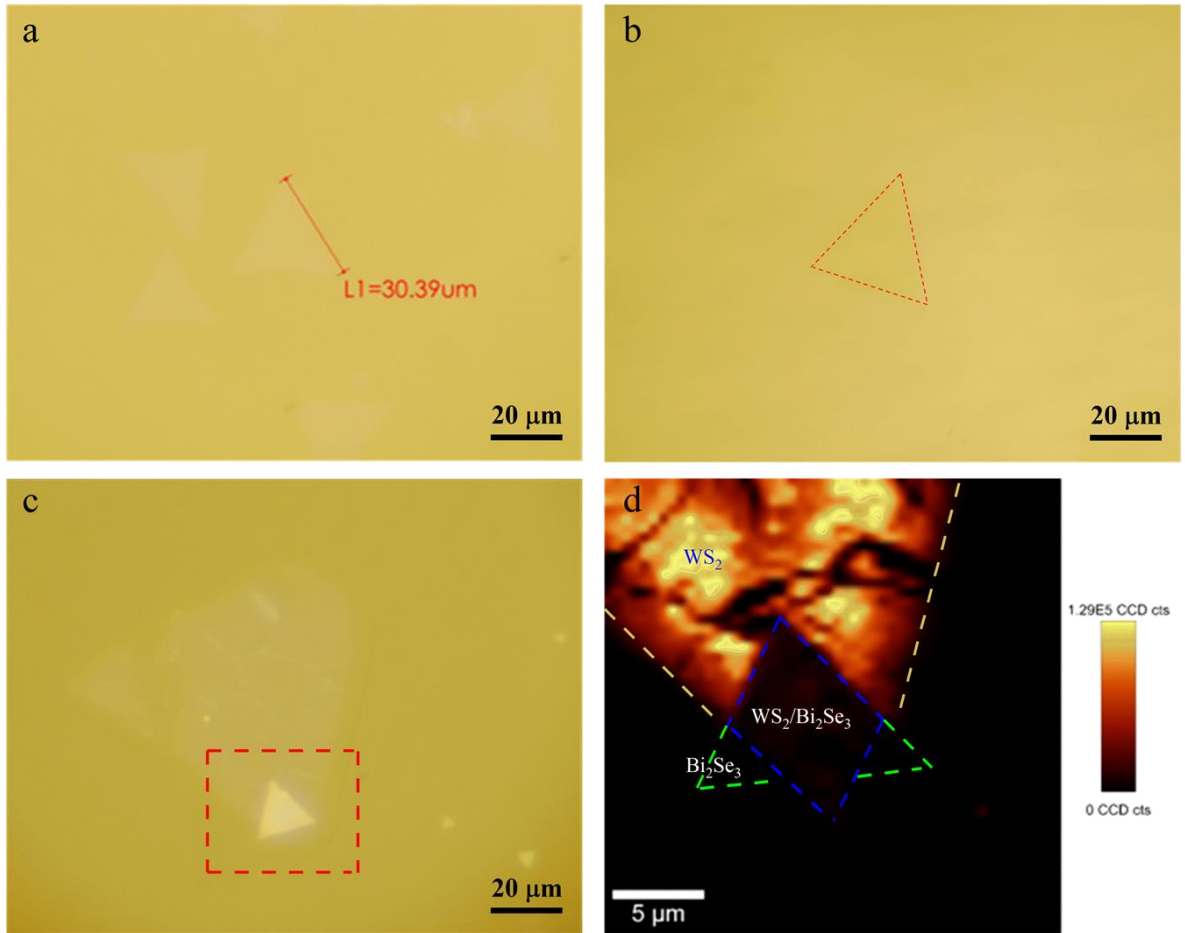


Figure S2. Optical image of half-wet transfer process from sapphire to mica. (a) Monolayer WS₂ grown on sapphire. (b) WS₂ lifted on PDMS. (c) The WS₂/Bi₂Se₃ heterostructure. (d) PL mapping of the region surrounded by red dashed lines in (c).

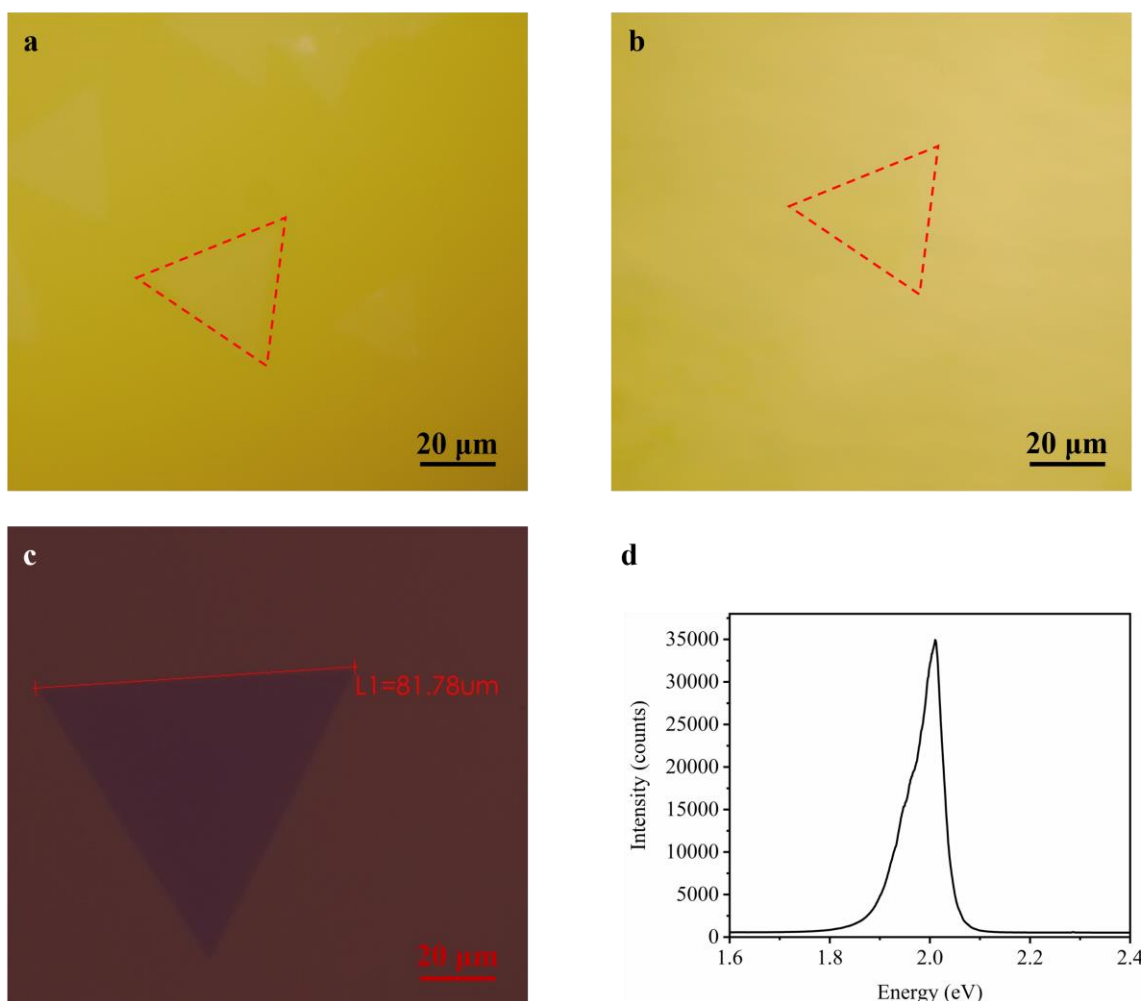


Figure S3. Optical image of half-wet transfer process from sapphire to SiO₂/Si. (a) Monolayer WS₂ grown on sapphire. (b) WS₂ lifted on PDMS. (c) WS₂ dropped onto SiO₂/Si. (d) PL spectra of WS₂ with high efficiency.

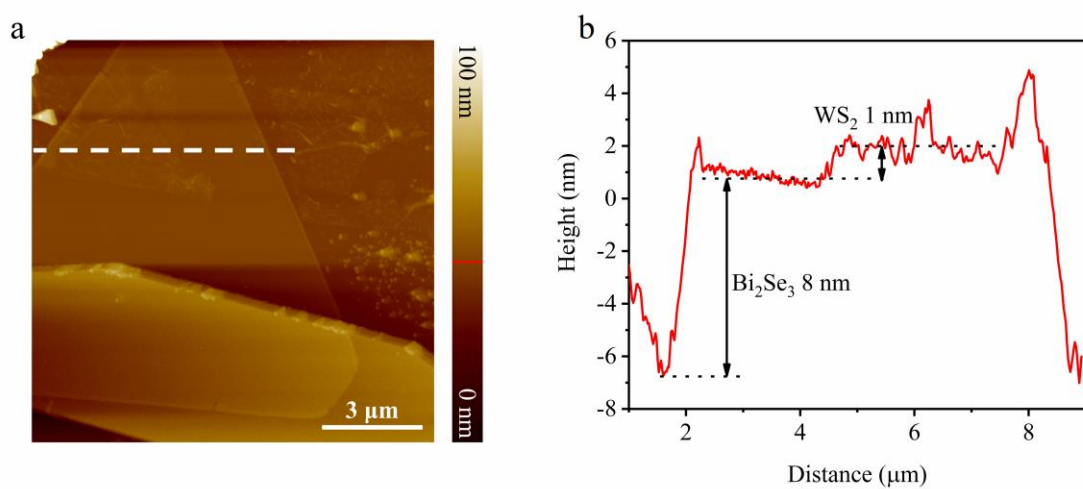


Figure S4. AFM of the WS₂/Bi₂Se₃ heterostructure. (a) AFM mapping of the WS₂/Bi₂Se₃

heterostructure and individual Bi_2Se_3 . (b) Height profile of the $\text{WS}_2/\text{Bi}_2\text{Se}_3$ heterostructure in (a) white dotted line.

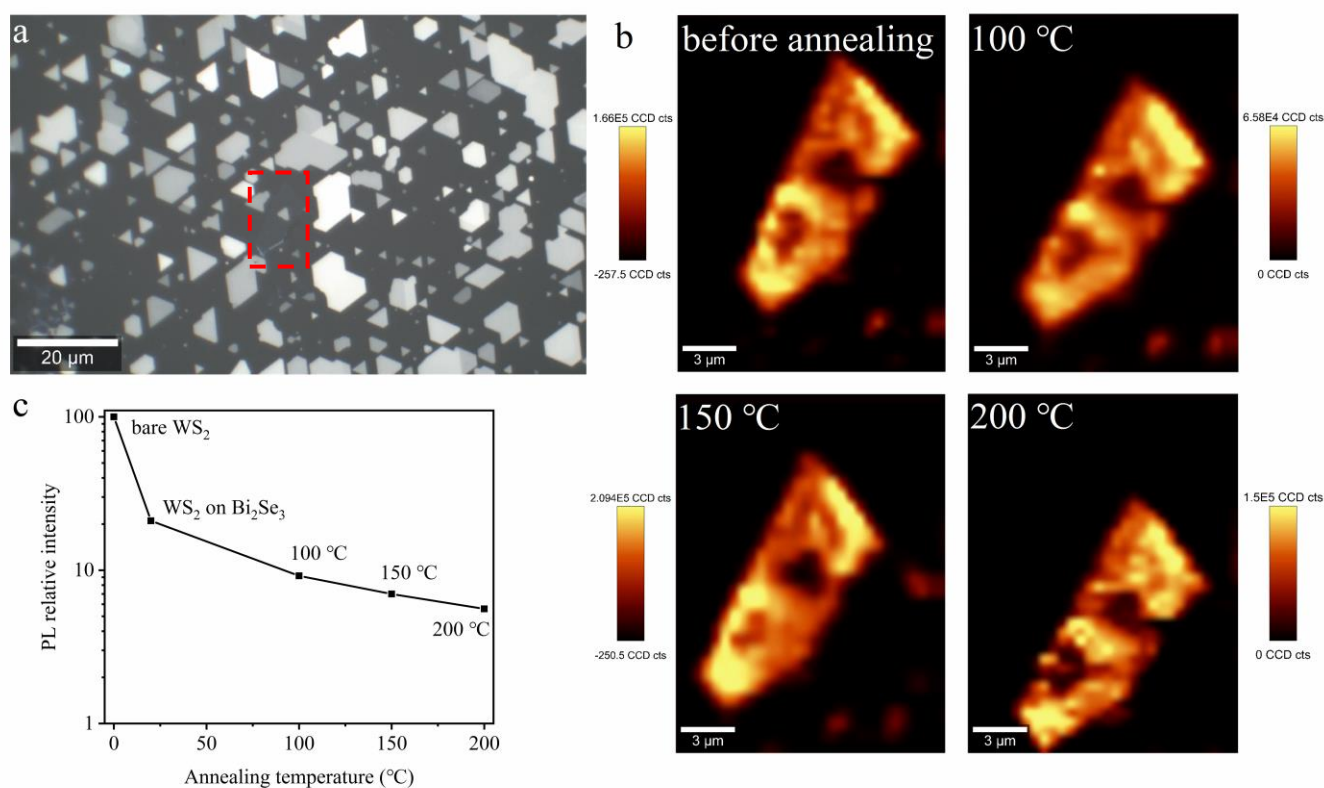


Figure S5. The evolution of PL intensity as a function of annealing temperature. (a) Optical image of selected $\text{WS}_2/\text{Bi}_2\text{Se}_3$ heterostructure, marked by red dotted rectangular. (b) PL mapping of selected region after annealing at different temperature. (c) PL relative intensity after annealing at different temperature.

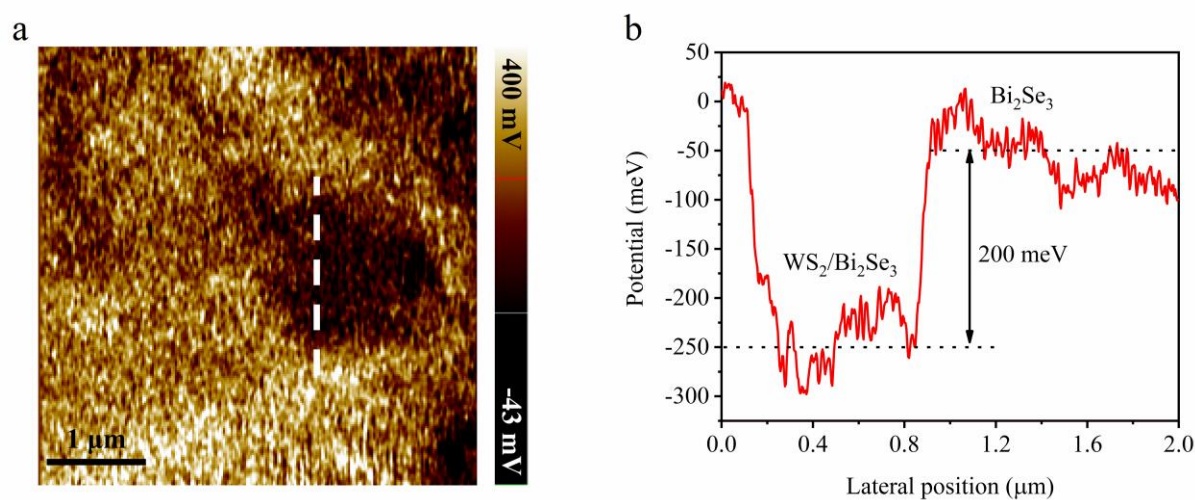


Figure S6. KPFM surface potential of the $\text{WS}_2/\text{Bi}_2\text{Se}_3$ heterostructure. (a) The surface potential mapping of the heterostructure and individual Bi_2Se_3 . (b) The surface potential profile across the sample corresponding to the dashed line in panel (a).

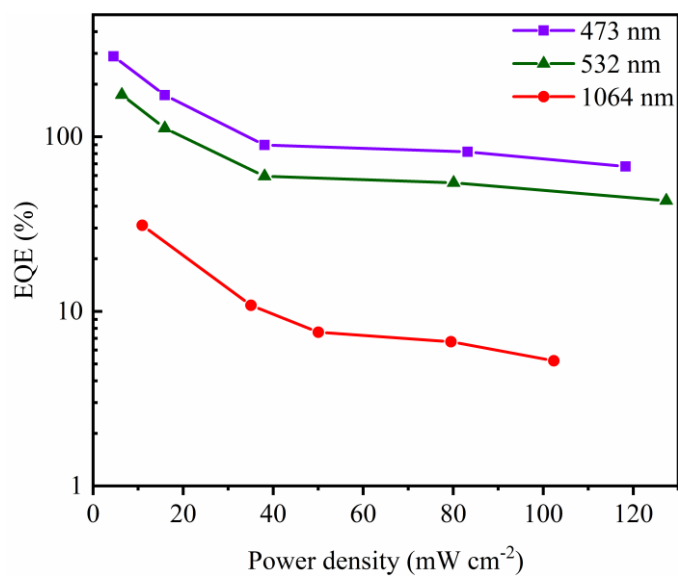


Figure S7. EQE of the $\text{WS}_2/\text{Bi}_2\text{Se}_3$ heterostructure device.

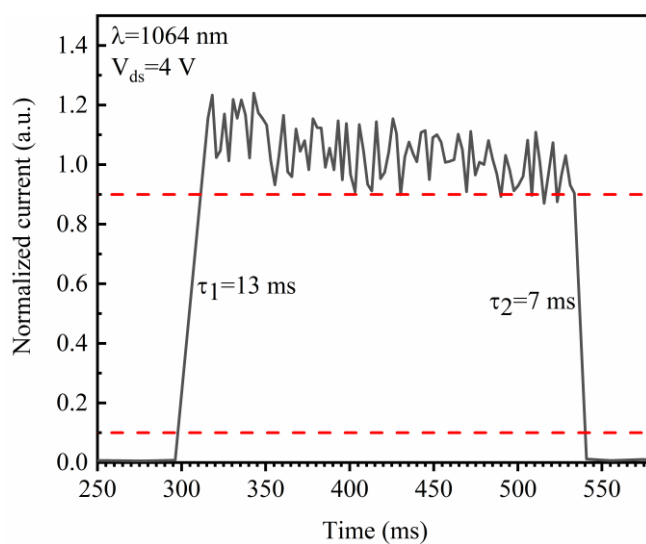


Figure S8. Response time curve of the heterostructure under 1064 nm laser illumination.

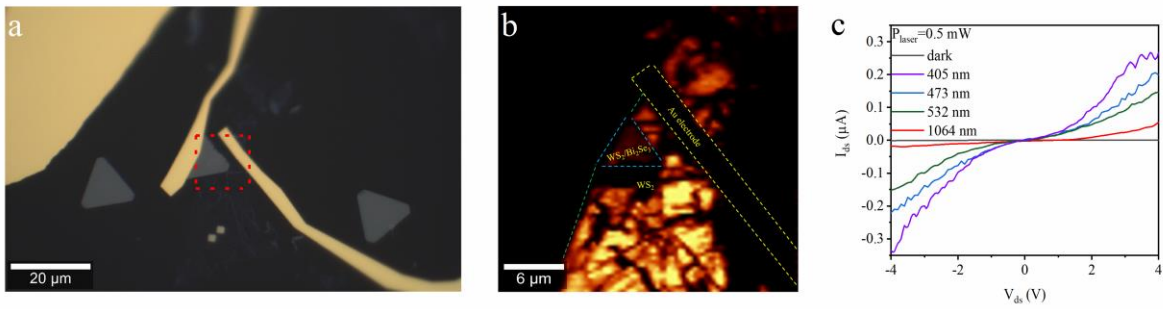


Figure S9. Optical image of the $\text{WS}_2/\text{Bi}_2\text{Se}_3$ heterostructure device and its photodetection performance. (a) Optical image of the heterostructure. (b) PL mapping of the region surrounded by red dashed lines in (a). (c) Broadband response of the device under different wavelength laser illumination at fixed laser power.

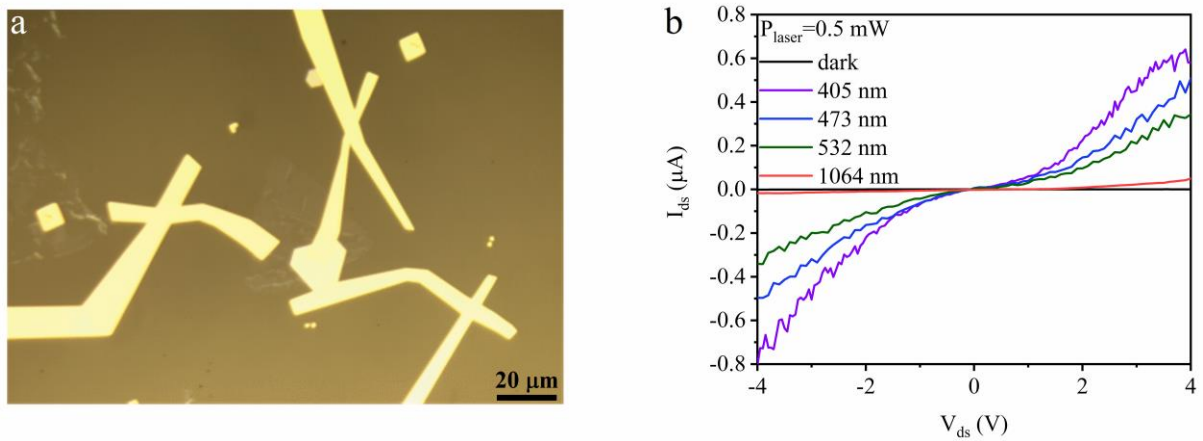


Figure S10. Optical image of the $\text{WS}_2/\text{Bi}_2\text{Se}_3$ heterostructure device and its photodetection performance. (a) Optical image of the heterostructure. (b) Broadband response of the device under different wavelength laser illumination at fixed laser power.